

Analysis of Airborne Magnetic and Radiometric Datasets for Geothermal Exploration, in North Central Nigeria

J.M., Sawuta¹; A.U., Sadiq²; A.A. El-Mansur³; M.A. Nyabam⁴; E.E. Udensi⁵;
A.A., Adetona⁶; C.I., Unuevho⁷; O.S., Ayanninuola⁸

^{1,2,3,4}Centre for Satellite Technology and Development (CSTD), National Space Research and Development Agency, Airport Road, Abuja

^{5,6,7}Department of Physics, Federal University of Technology, Minna

⁸Department of Physics, Nasarawa State University, Keffi

Publication Date: 2025/03/31

Abstract: This study uses high-resolution aeromagnetic and radiometric datasets to assess Nasarawa State's geothermal potential. Analysis was done on six 55 km by 55 km aeromagnetic data sheets. Heat flow, the geothermal gradient, and Curie point depth (CPD) were among the geothermal depth parameters that were determined in the study. The average CPD value was 21.22 km, with a range of 10.14 km to 86.75 km. Heat flow estimates ranged from 62.66 mW/m² to 211.64 mW/m², with an average of 125.12 mW/m², while the geothermal gradient varied from 6.6°C/km to 57.19°C/km, averaging 33.18°C/km. Geothermal energy sources that have shallower CPD and higher heat flow are probably promising. The average radiogenic heat value was 1.87 μW/m³, with a range of 1.48 to 2.32 μW/m³. Overall, the study suggests that geothermal potential is high in the central basement region, where alteration zones appear more concentrated in the northeastern and northwestern parts. Generally, from the analysis of this research, Geothermal potential are promising around central basement of the area where there are likely of higher alteration zones located around the north eastern and north western region.

Keywords: Geothermal, Airborne Radiometric, Airborne Magnetic, Radiogenic and Geothermal.

How to Cite: J.M., Sawuta; A.U., Sadiq; A.A. El-Mansur; M.A. Nyabam, E.E. Udensi; A.A., Adetona; C.I., Unuevho; O.S., Ayanninuola. (2025). Analysis of Airborne Magnetic and Radiometric Datasets for Geothermal Exploration, in North Central Nigeria. *International Journal of Innovative Science and Research Technology*, 10(2), 2453-2466. <https://doi.org/10.38124/ijisrt/25feb581>.

I. INTRODUCTION

Geophysical techniques such as magnetic and radiometric methods are useful in assessing geothermal energy potential. These approaches help detect underground geological structures by studying differences in the magnetic field of Earth brought on by the crust's varying degrees of magnetization (Udensi et al., 2016). The aeromagnetic method is particularly valuable in geothermal studies because it identifies both deep and shallow magnetic sources. These findings assist in estimating Curie point depth (CPD), which plays a key role in determining geothermal heat flow through power spectral analysis (Udensi et al., 2016).

Aircraft-mounted scanners that capture digital radiation emissions from the Earth's surface are used to gather airborne radiometric data across large areas. Radiation from elements that exist naturally, such as potassium (K), thorium (Th), and uranium (U) is measured using these scanners. which exist in varying amounts in different rock types. As rocks break

down, the concentrations of these elements influence the soil composition (Shi & Butt, 2004). Radiometric data often correlates with the underlying bedrock formations (Gunn et al., 1997). According to Fugro Airborne Surveys (1961), approximately 90 % of gamma rays originate from the top 30 - 45 cm of soil. The emission levels of K, Th, and U are instrumental in mapping soil properties and regolith (Gunn et al., 1997). Furthermore, these measurements help distinguish between different lithological units based on their radioelement concentrations (Anderson & Nash, 1997; Graham, 1993; Jaques et al., 1997; Charbonneau et al., 1997). Among airborne geophysical techniques, gamma-ray spectrometry is particularly effective for mapping surface geology (Darnley, 1990).

Beyond geothermal exploration, radioactive heat assessments have applications in uranium prospecting (Grasty, 1979), investigating sedimentary formations for mineral exploration (Mero, 1960), oil and gas exploration (Myers & Bristow, 1979; Davies et al., 1996), and radioactive

contamination detection (Rybach *et al.*, 1995; Sanderson *et al.*, 1989). The decay of radioactive materials is the main source of heat in the Earth's crust in rocks, although other localized sources may contribute (Jessop, 1990). Scientists have estimated radioactive heat production using laboratory measurements of radioelement concentrations (Fernández *et al.*, 1998) or gamma-ray logs (Bücker & Rybach, 1996) to derive accurate heat values. Airborne gamma-ray data has also been employed in assessing radioactive heat generation (Salem *et al.*, 2005; Richardson & Killen, 1980; Thompson *et al.*, 1996).

The study area for this research was chosen due to the presence of subsurface heat and a natural warm water spring, indicating high-temperature conditions. This makes the area particularly suitable for exploring geothermal potential, highlighting the importance of this research.

II. LOCATION AND GEOLOGY OF THE STUDY AREA

This study area was selected due to evidence of subsurface thermal activity and the presence of a natural warm spring, indicating a high-temperature environment between longitudes 07.30° E and 09.00° E and latitudes 08.00° N and 09.00° N. It crosses the middle Benue trough in North Central Nigeria as well as portions of the basement complex covering sections of Nasarawa State and its neighboring regions. The area extends over approximately 18,150 km² and is represented by six airborne magnetic and radiometric maps. These maps correspond to sheets 208, 209, 210, 229, 230, and 231, which include the locations of Keffi, Akwanga, Wamba, Udegi, Doma, and Lafia, respectively.

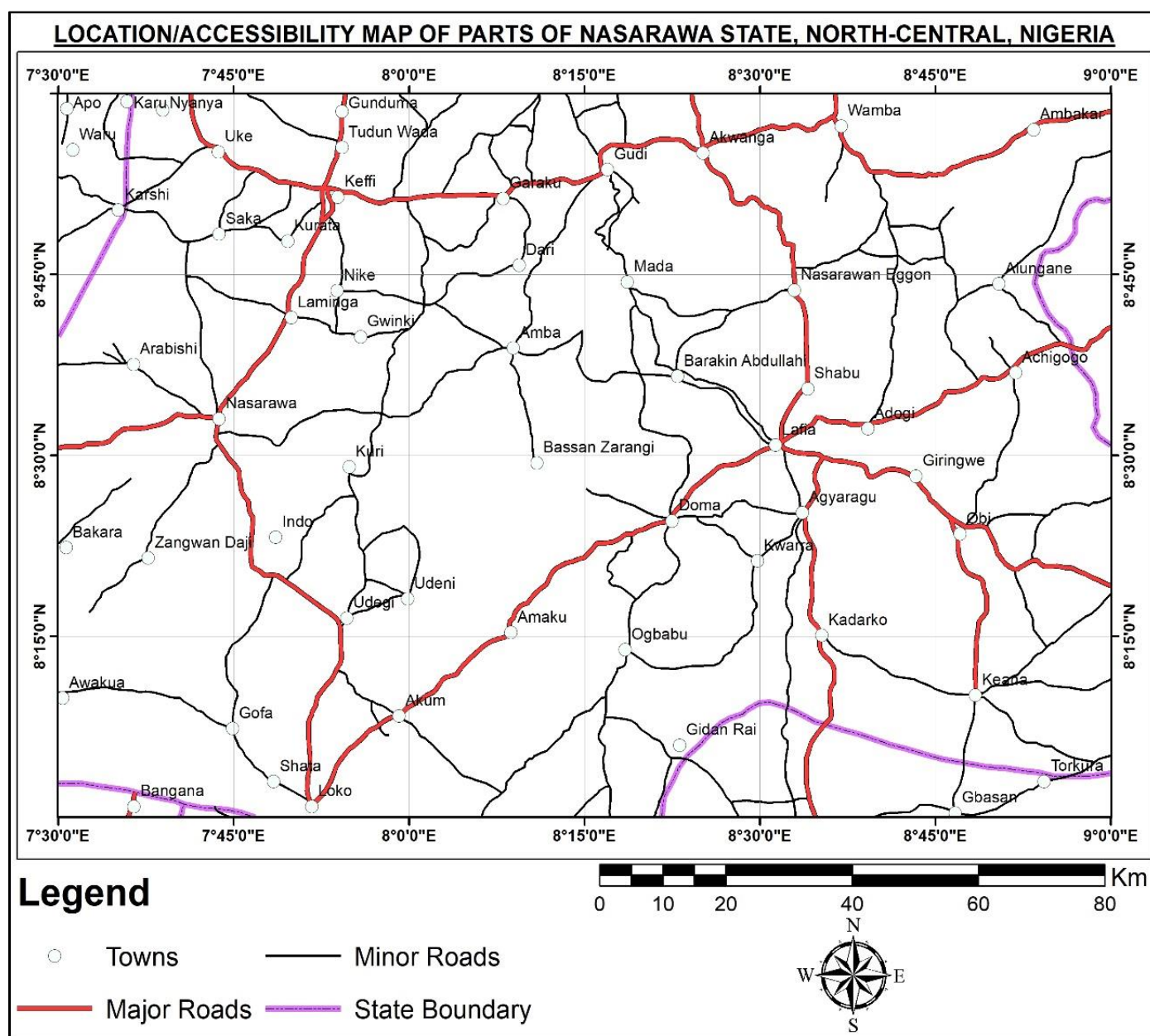


Fig 1: Map of the Study Area Showing Towns, Minor and Major Roads and State Boundary

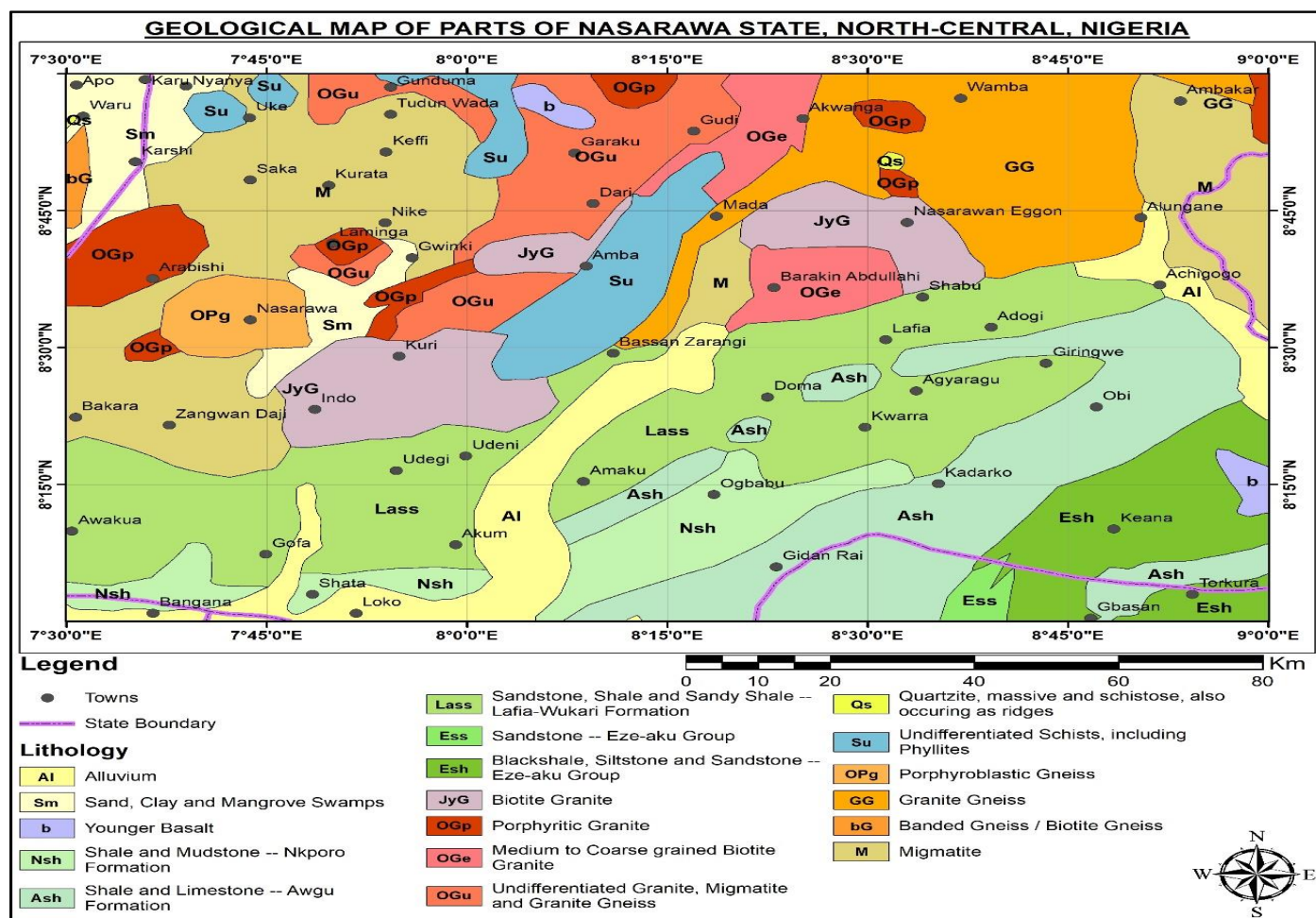


Fig 2: Geological Map of the Study Area, Modified from NGS, (2006)

The study area is well-connected and easily accessible, with major road networks such as the Keffi-Abuja Expressway, Keffi-Abaji-Lokoja Expressway, Keffi-Kaduna Expressway, Lafia-Makurdi Expressway, and Akwanga-Jos Expressway. In addition, a railway line stretches nearly the entire length of the area, running from north to south. The region's vegetation and climate are characteristic of the Guinea Savannah.

Geologically, the area (Figure 2) is composed of both the Middle Benue Trough and the basement complex and sedimentary basins in North-Central Nigeria. Rock types found in Schist, porphyritic granite, banded gneiss/biotite gneiss, migmatite-gneiss, and other minerals are found in the basement complex. medium to coarse-grained biotite undifferentiated granite, migmatite, granite gneiss, and undifferentiated schist, including phyllites. The sedimentary basin, on the other hand, consists of shale, sandstones from the Eze-Aku Group, shale and mudstones from the Nkporo Formation, and deposits of sand, clay, and quartzite. The rocks in the area have undergone multiple phases of deformation, with ages ranging from Precambrian to Pan-African.

III. MATERIALS AND METHODS

A. Gathering and Analyzing Data

Six sheets—208 (Keffi), 209 (Akwanga), 210 (Wamba), 229 (Udege), 230 (Doma), and 231 (Lafia)—cover the research region. Fugro Airborne Surveys measured and obtained the sheets for the 1:100,000 scale, Nigerian Geological Survey Agency (NGSA). The primary source of data used to investigate the magnetic abnormalities in the area was these sheets. The survey was conducted using North-South flight lines spaced three kilometers apart, with an average flying altitude of 80 meters above sea level. Using distance between flight lines of around 3 km and digitizing contour maps of overall magnetic strength and shape intervals of 0.0271 units, magnetic data was acquired.

For the radiometric data, information was extracted from 12 radiometric sheets in all. The radiometric scan was carried out at an altitude of 80 feet in the air meters, with flight lines spaced 500 meters apart and tie-lines spaced 5,000 meters apart. This data was used to complement the magnetic analysis and provide a comprehensive understanding of the study area.

Assembling The first step is to create a composite map from the nine aeromagnetic maps that cover the survey area. in the current investigation (Figure 3).

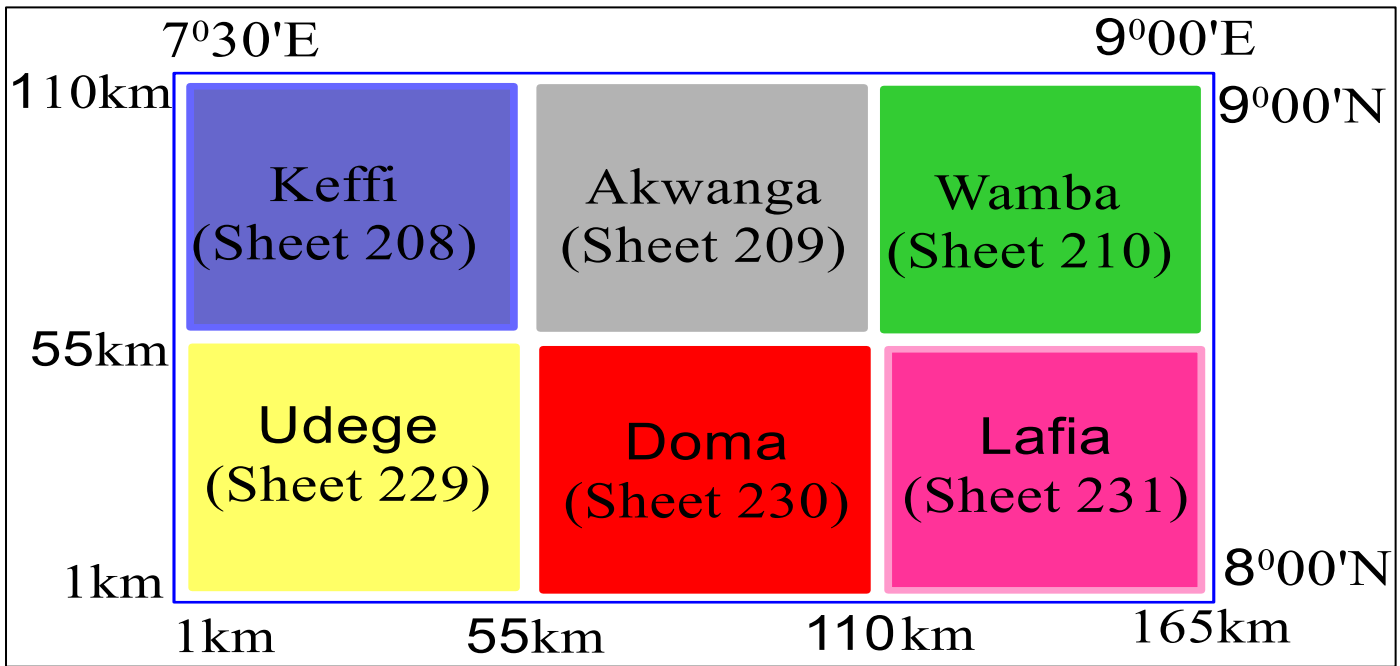


Fig 3: The Composite Aeromagnetic Map

Likewise, Each of the three radiometric elements uranium (U), thorium (Th) and potassium (K) has its own map was created by contouring the six radiometric data sheets. One radiometric heat map was subsequently created from the heat calculations.

B. Theory of Spectral Analysis for geothermal heat flow

The depth to which the temperature of Curie is attained is frequently estimated using magnetic techniques. There are two main methods for figuring out how deep magnetic sources are. While the second method concentrates on the first approach looks at the shape of individual magnetic anomalies (Bhattacharyya and Leu, 1975), whereas the second way analyzes the statistical features of magnetic anomaly patterns (Spector and Grant, 1970). Both methods link converting spatial data into the frequency domain in order to determine the spectrum of magnetic anomalies to the depth of the magnetic source (Tanaka et al., 1999). The Spector and Grant method is particularly effective for studying magnetic anomalies on a regional scale.

The idea behind the spectral depth approach is that the magnetic field that is detected at the surface of the Earth is a sum of magnetic signals from different depths. It is possible to assess the average depth of magnetic sources by examining the surface field's power spectrum. The characteristic depth of the magnetic basement can also be ascertained with this method. The steepest part of the power spectrum, which is assumed to reflect magnetic contrasts at the basement surface, is analyzed to derive depth estimates. These estimates are obtained by calculating the power spectrum for each data window, with each window centered on a grid subset. Overlapping these windows ensures a robust set of depth estimates.

For this investigation, the Spector and Grant (1970) technique was used in accordance with Tanaka et al. (1999)

methods. Spectral analysis techniques are used to isolate the effects of various parameters in the recorded magnetic anomaly field in order to determine the Curie Point Depth. The inverse problem is made more difficult by the fact that the signal from a magnetic body's surface typically obscures the signal from deeper layers at all wavelengths (Blakely, 1995). In essence, the Spector and Grant approach uses the slope of the log power spectrum to determine the average depth to the top of a set of magnetized rectangular prisms. The Bhattacharyya and Leu method, on the other hand, uses the centroid of a single anomalous body to calculate the distance to a causal factor. These ideas were combined and improved upon by Okubo et al. (1985) to create a regional geomagnetic interpretation algorithm that is particularly suitable for geothermal exploration. They presented a two-dimensional modeling method that uses average ensemble features to determine the depth of a single block's foundation. Their approach uses the slope of the radially averaged frequency-scaled power spectrum to determine the depth to the centroid (Z0).

$$[\ln(\frac{p(\omega)}{k})] = A - |k|Z_0$$

$[\ln(\Phi(\omega)1/2/\omega)]$ Is the low-wave number zone, and Zt is the depth to the top (Zt) from the slope of the radially averaged power spectrum (RAPS), where ω indicates radial frequency.

Equation (1) illustrates the relation that is used to determine the centroid depth from the low wave number portion of the wave number-scaled power spectrum:

$$\ln(p(k) 1/2 /k = A - |k|Z_0 \tag{1}$$

Where (k) is the power spectrum, k is the wave number, A is a constant, and Z0 is the centroid depth. Similarly, the slope of the power spectrum's mid-to-high wave number area

is utilized to calculate the depth to the top of the magnetic sources using the relationship in equation 2:

$$\ln(p(k) / 2) = B - |k|Z_t \quad (2)$$

Z_t represents the depth to the top of the magnetic sources in this instance, while B is a constant. A deeper approximation of the magnetic bottom, which is often sought, is obtained by fitting the slope to the higher wave number portion of the spectrum (Tanaka et al., 1999; Ravat et al., 2007). The equation in (3) is used to calculate the Curie Point Depth (CPD), or depth to the bottom of the magnetic source (Z_b), as stated by Okubo et al. (1985).

$$Z_b = 2Z_c - Z_t \quad (3)$$

The previously stated method is quite similar to Tanaka et al.'s (1999) method, which uses both the high and low wavenumber components of the Radially Averaged Power Spectrum (RAPS). To find the top boundary of the magnetic source (Z_t), they fitted a straight line to the high-wavenumber portion of the RAPS, $\ln(\Phi\Delta T/K) / 2 \ln(\Phi\Delta T/K) / 2$. By aligning a straight line with the frequency-scaled low-wavenumber area RAPS, which is denoted as $\ln(\Phi\Delta T/K) / 2 / k \ln(\Phi\Delta T/K) / 2 / k$, the centroid (Z_0) was also found. In this case, the wavenumber is k , and the power density spectrum is represented by $\Phi\Delta T$.

To facilitate in-depth spectrum research, the study region was separated into twenty overlapping pieces, each measuring 55 km by 55 km. The residual data for each block was subjected to power spectrum analysis, where the logarithms of spectral energies were displayed against frequency. The generated graphs displayed linear segments, the slopes of which matched the depths of the ensembles of magnetic sources responsible for the anomalies.

Every block was transformed into a power spectrum by statistical processing. A logarithmic scale was then used to illustrate the data against frequency. In these graphs, the data points from a set of sources will create a straight line with a constant slope if they have a similar depth.

However, if the sources are at different depths for example, shallow volcanic sources overlying a deeper basement—the plot will display segments with varying slopes. The steepness of these slopes provides an indication of the depth of the sources. This process was repeated for all twenty blocks to estimate the depths of both shallow (Z_t) and deep (Z_b) magnetic sources. Finally, the Curie Point Depth for each block was calculated using the formula given in equation (4).

Fourier's Law provides an equation that expresses the value of the geothermal heat flow.

$$q = \left[\frac{dT}{dz} \right] \lambda \quad (4)$$

Udansi et al. (1999) estimated geothermal heat flow using the same equation, where q is the heat flow and λ is the thermal conductivity coefficient and Tanaka and Ishikawa (2005). Since sandstone predominates in the region they studied, Reiter et al. (1985) determined thermal conductivity values for several rock types, settling on an average of 1.8 W/m °C. However, the average thermal conductivity is assumed at 3.7 W/m °C for this study, which focuses mostly on igneous and granitic rocks. The following formula can be used to get the Curie temperature (θ) from the temperature gradient (dT/dz) and the Curie point depth (Z_b):

$$\theta = \left[\frac{dT}{dz} \right] Z_b \quad (5)$$

Combining equations (4) and (5) allowed for the calculation of the geothermal heat flow values.

$$q = \lambda \frac{\theta}{Z_0} \quad (6)$$

C. Theory of Airborne Radiometric Data

Soil mapping and, to a lesser extent, structure mapping are two of the many uses for radiometric data. However, by analyzing the spatial relationship between radiometric data and the underlying rock formations, it is primarily used for mapping lithological units and finding modifications (Gunn et al., 1997). This involves measuring naturally occurring radioactive elements present in the minerals that compose rocks and soils (Telford et al., 1990). The collected data is used to create images, which are then analyzed and interpreted to gain geological insights. These images and maps are typically interpreted visually to identify lithologies, characterize rock types, and outline potential surface geological structures. Areas with high concentrations of radiometric elements or irregular low magnetic readings are often interpreted as indicators of mineral deposits or rock alterations (Gunn et al., 1997).

D. Radiometric Data Processing

The radioactive heat values were calculated using an empirical method developed by Rybach (1976) based on the energy produced by the Alpha, Beta, and Gamma decay of rocks (Salem and Fairhead 2011). This is how the formula is written:

$$A(\mu W/m^3) = \rho(0.0952 C_{Cu} + 0.0256 C_{Th} + 0.0348 C_K) \quad (7)$$

In this case, A stands for radioactive heat, while ρ , which was taken from Telford et al. (1990), is the rock's density. The average rock density employed in this study was 2.8 kg/cm³.

The levels of potassium (in percentage), the concentrations of potassium (K), thorium (Th), and uranium (U) are used to indicate thorium (in parts per million), and uranium (in parts per million). The methodology used in this study is very similar to that of Salem et al. (2005), who meticulously specified the boundaries of rock units to prevent overlap while allocating densities and associated radioelement values to each rock unit.

According to the radiometric data obtained during the study the three natural radionuclide distributions, corresponding concentrations of uranium (eU), potassium (K), and thorium (eTh) were determined. When compared to their initial bedrock composition, weathering activities can drastically alter these radioelements' concentration and distribution. The gamma rays near the surface are associated with worn minerals, geochemical changes, and the mineralogical composition of the underlying bedrock. The ratios of these radioelements (eU/K, eU/Th, and eTh/K) are listed in Chapter 4. For further study, the "tannery map"—a composite picture of the radioelements that integrates information for K (%), eU, and eTh was also created.

IV. RESULTS AND DISCUSSION

The Map of Total Magnetic Intensity (Figure 4a) reveals a mix of high (H) and low (L) magnetic signatures, which align with the features shown in the digital elevation map

(Figure 4b). The magnetic anomalies vary in shape and size, with intensity values ranging from 31,943.3 nT to 32,111.5 nT. Areas with low magnetic intensity, depicted in green-blue, have values between 31,943.3 nT and 32,036.6 nT. Medium-intensity zones, shown in yellow-orange, fall within the range of 32,039.5 nT to 32,059.4 nT. High magnetic intensity regions, highlighted in red-pink, exhibit values from 32,061.8 nT to 32,111.5 nT.

The low magnetic intensity areas, such as Lafia, Doma, Adogi, Keana, Shabu, Gofa Akum, Loko, and Torkura, suggest the presence of rocks with lower magnetic concentrations. On the other hand, the high magnetic intensity zones in the northern part of the study are including Akwanga, N/Eggon, Wamba, Nasarawa Eggon, Keffi, Gunduma, Tudun Wada, Garaku, and Dari—are linked to rocks with higher magnetic concentrations. This contrast in magnetic signatures provides valuable insights into the geological composition of the region.

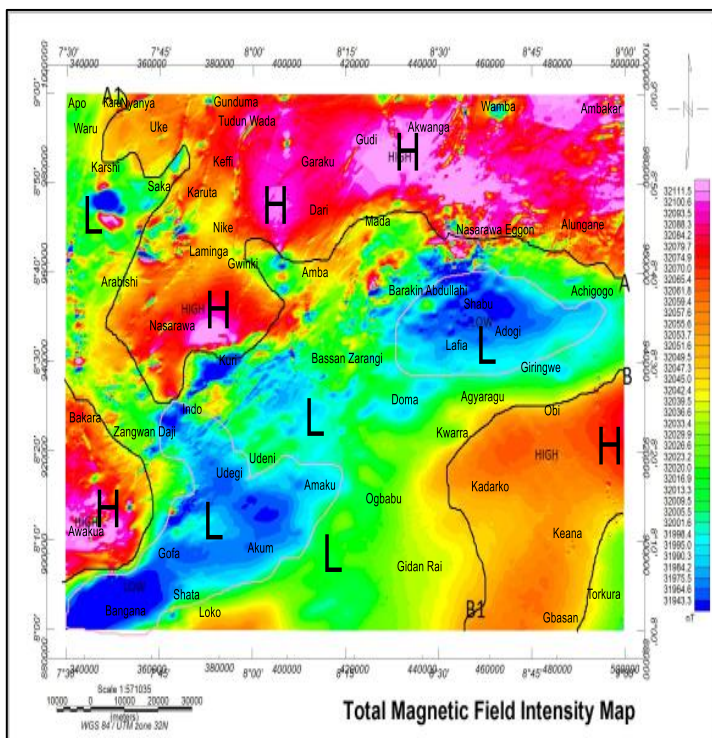


Fig 4(a): TMI Map of the Study Area

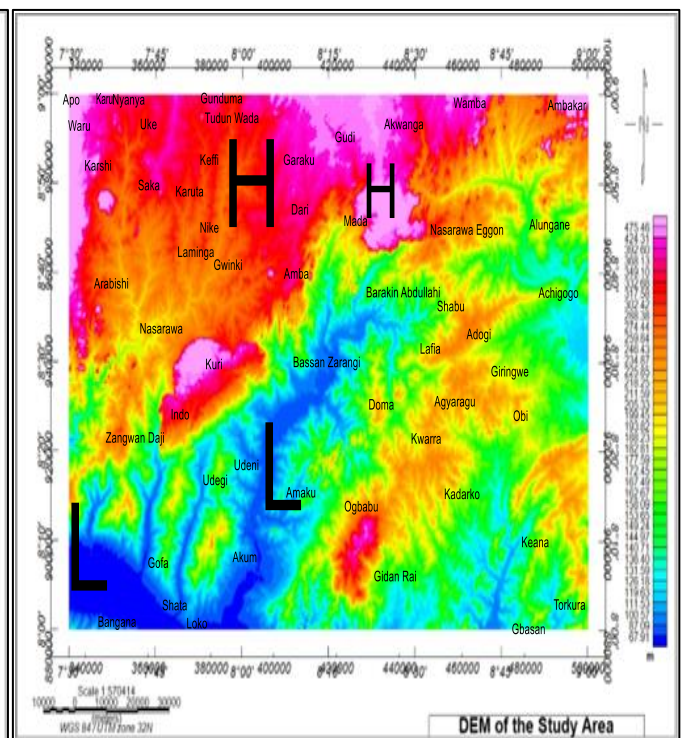


Fig 4(b): DEM of the Area

The digital elevation map (Figure 4b) highlights areas of both high (H) and low (L) elevation across the study region. Elevations range from 67.91 meters to 475.46 meters, with an average elevation of 271.69 meters. Much of the area is dominated by highland regions (marked as H in Figure 3a). The higher elevations at northern region of the research area are largely linked to granitic rocks, which belong to the basement complex and are responsible for the strong magnetic signatures seen in Figure 4a. On the other hand, the lower elevations, shown in green in Figure 3a, align with sedimentary formations such as sandstone, shale, limestone,

and mudstone. This contrast in elevation and rock types provides a clear picture of the region's geological diversity.

A. Residual Magnetic Intensity (RMI) Map

The values of the regional fields are deducted from the total magnetic data to determine the residual values. The resulting residual map is displayed in Figures 5a and 5b. It's worth noting that most geophysical interpretations focused on identifying features within the study area rely on residual maps. In this study, the residual magnetic intensity across the area was found to vary between -93.5 nT and 95.4 nT.

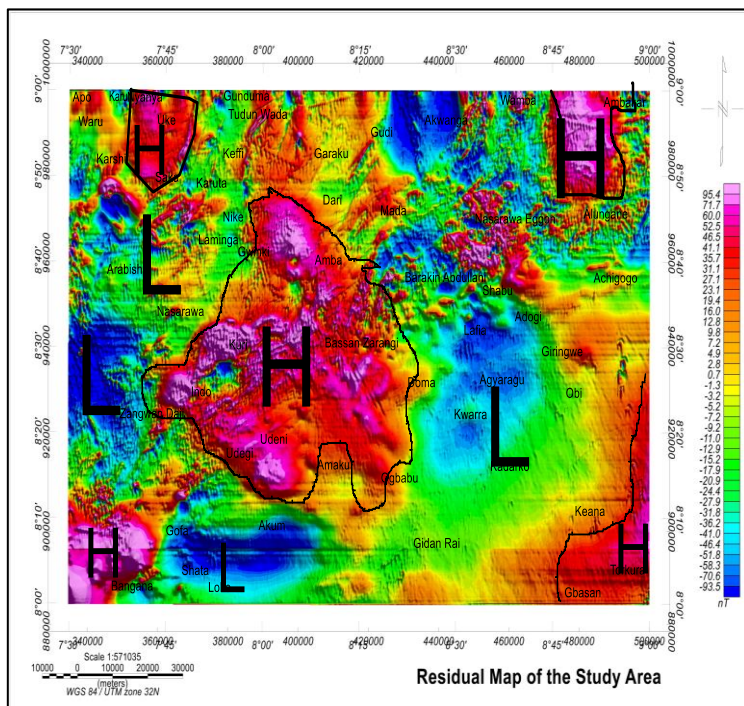


Fig 5(a): RMI Map of the Area

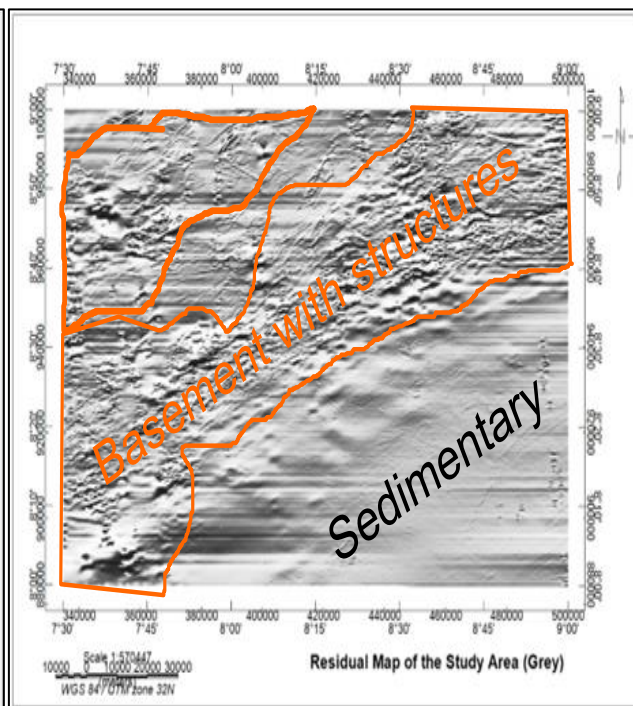


Fig 5(b): RMI Map of the Area (Grey)

The residual anomalies in this study area closely resemble those seen in the total magnetic field map (Figure 4a). However, certain anomalies visible on the residual map are not as apparent on the total magnetic field intensity map. These anomalies might still be present but are likely obscured by the more dominant regional trends.

B. Geothermal Heat Production Analysis

The findings from the spectral plots (Figures 6 and 7) are outlined in Table 1. The table includes details about each block, along with the depths to the bottom (Z_0Z_0) and top (Z_tZ_t) of the magnetic sources. Using equations (5) and (6), the Curie Point Depth (CPD) and Geothermal Heat Flow (GHF) were also calculated and included in the summary.

Table 1: Spectral Analysis Results Obtained from Twenty (20) Blocks

S/N	Sections	Longitudes (°C)	Latitude (°C)	Bottom Depth, (km)	Top Depth, (km)	Curie Point Depth, (km)	Geothermal Gradient (°C/km)	Geothermal Heat Flow (mWm ⁻²)
1	A	7.50-8.00	8.50-9.00	10.70	1.70	19.70	29.44	108.93
2	B	7.75-8.25	8.50-9.00	10.40	1.51	19.29	30.07	111.25
3	C	8.00-8.50	8.50-9.00	8.06	1.14	14.98	38.72	143.26
4	D	8.25-8.75	8.50-9.00	14.00	1.67	26.33	22.03	81.50
5	E	8.50-9.00	8.50-9.00	17.50	0.75	86.75	06.69	62.66
6	F	7.50-8.00	8.33-8.83	8.50	1.46	15.54	37.32	138.01
7	G	7.75-8.25	8.33-8.83	6.52	2.90	10.14	57.19	211.64
8	H	8.00-8.50	8.33-8.83	7.67	0.94	14.39	40.31	149.13
9	I	8.25-8.75	8.33-8.83	14.20	1.46	26.94	21.53	79.66
10	J	8.50-9.00	8.33-8.83	10.70	2.45	18.95	30.61	113.25
11	K	7.50-8.00	8.16-8.67	8.83	2.72	14.94	38.82	143.64
12	L	7.75-8.25	8.16-8.67	9.78	1.31	18.25	31.78	117.59
13	M	8.00-8.50	8.16-8.67	8.79	1.93	15.65	37.06	137.12
14	N	8.25-8.75	8.16-8.67	10.50	1.66	19.34	29.99	110.96
15	O	8.50-9.00	8.16-8.67	11.00	2.71	19.29	30.07	111.25
16	P	7.50-8.00	8.00-8.50	7.59	3.96	11.22	51.69	191.27
17	Q	7.75-8.25	8.00-8.50	8.98	3.95	14.01	41.39	153.18
18	R	8.00-8.50	8.00-8.50	11.60	3.57	19.63	29.55	109.32
19	S	8.25-8.75	8.00-8.50	13.40	3.32	23.48	24.70	91.31
20	T	8.50-9.00	8.00-8.50	9.35	3.09	15.61	37.16	137.48
Minimum				6.52	0.75	10.14	6.69	62.66
Maximum				17.50	3.96	86.75	57.19	211.64
Average				10.40	2.21	21.22	33.18	125.12

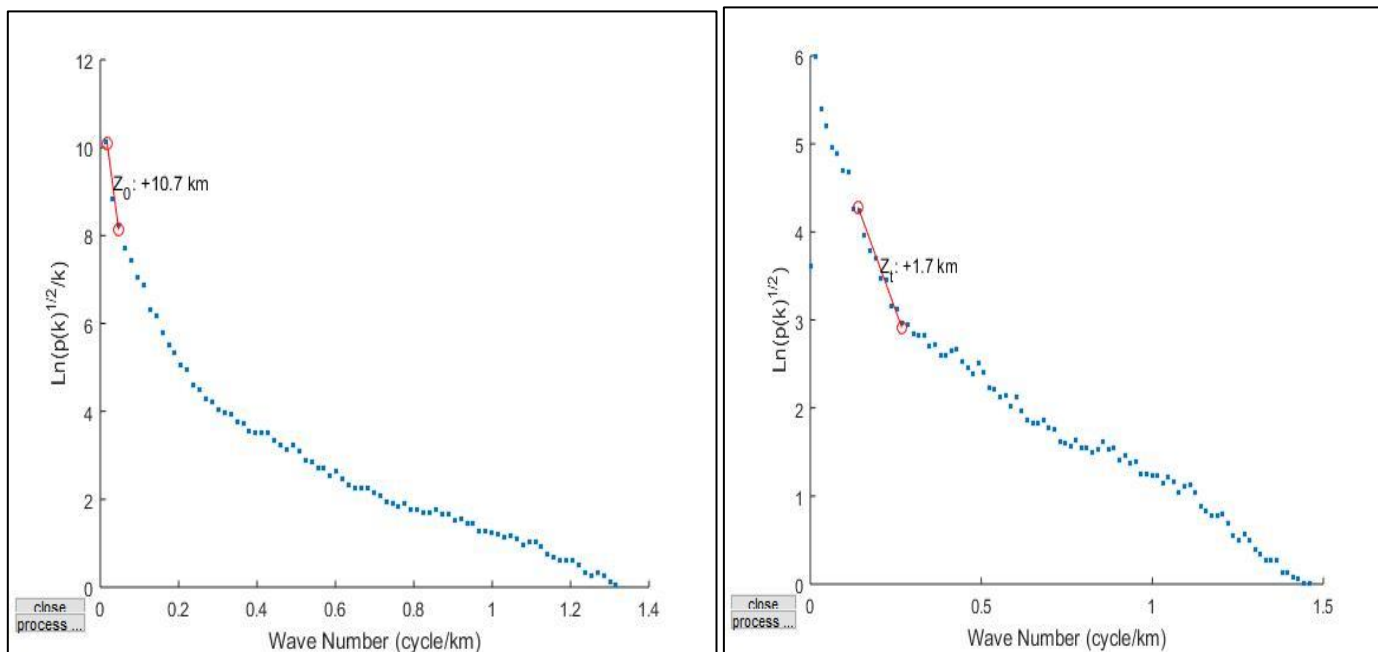


Fig 6: Spectral Plot of Block A

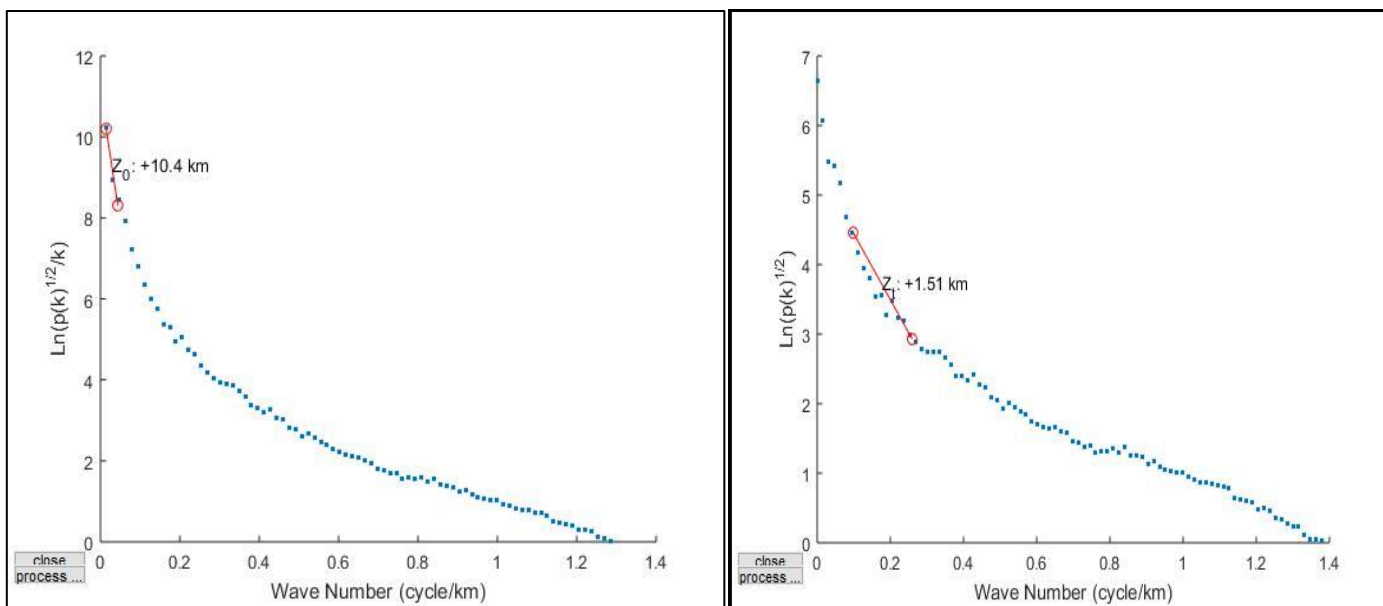


Fig 7: Spectral Plot of Block B

The typical depth to the top of magnetic sources in the study area is 21.22 km, with a range of 0.75 km to 3.5 km, according to the findings (Table 1).

Figure 8 displays the findings of the Curie Point Depth (CPD) study for the study region, indicating that the average Curie isotherm depth is 21.22 kilometers. with variations ranging from 10.4 km to 86.75 km. With the exception of the far northeastern region, where deeper values are shown, the majority of the region is covered by the shallowest depths, according to a closer examination Showing the depth map of

Curie points. The total Curie point depths are typically less than 15 km, indicating that the entire area is within a volcanic and geothermal field, since the Curie point depth is heavily influenced by geological circumstances. (Tanaka et al., 1999). With contours in Figure 10 going northeast-southwest, the middle region exhibits comparatively greater CPD values, whereas the southwest portion of the research area has the shallowest Curie point depths. It is advised that more geothermal exploration and thorough research be done throughout the region in light of these discoveries.

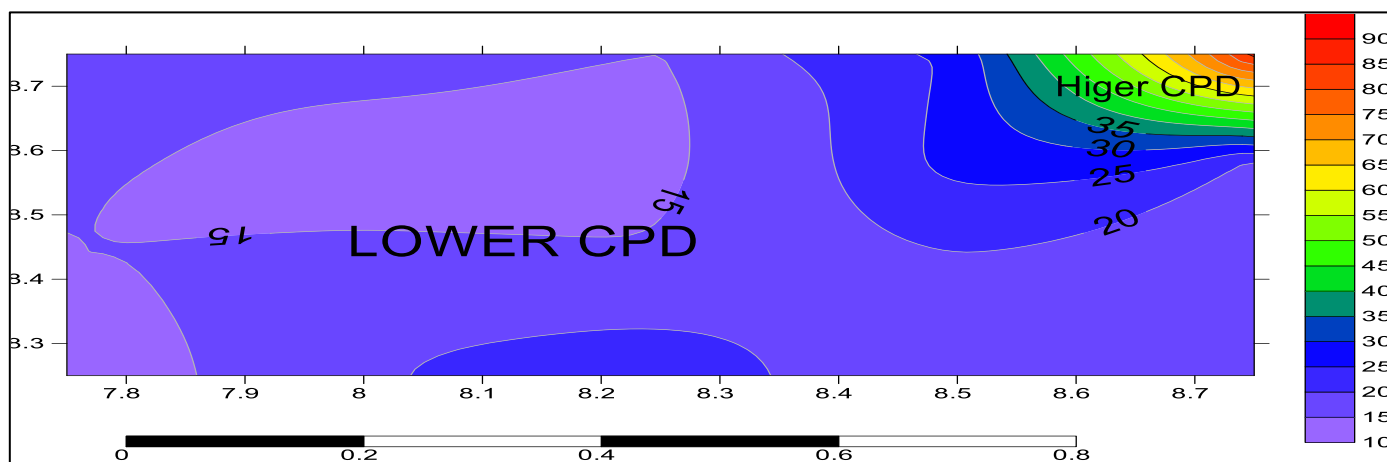


Fig 8: Distribution Map Showing Curie Point Depth (CPD)

Variations in the geothermal gradient throughout the investigated site were identified by using the calculated Curie depths and the Curie temperature of 580°C (Nwankwo et al., 2011; Chinwuko et al., 2012). The average geothermal heat flow (Figure 9) is 125.12 mW/m², with a range of 62.66 mW/m² to 211.64 mW/m². According to Onwuemesi (1997), Anakwuba and Chinwuko (2015), and Usman et al. (2016), this range is in line with usual values for continental crust. The study's findings support the notion that Curie depths are

direct indicators of the thermal structure by showing that both heat flow and the Curie point depth are strongly correlated with the local geology. Additionally, Nwankwo et al. (2011) noted that igneous and metamorphic rocks, which have high thermal conductivities, are frequently associated with areas with high heat flow values. The research area shows this tendency, especially in the Indo, Nasarawa, and Kuri regions, which have a lot of geothermal potential.

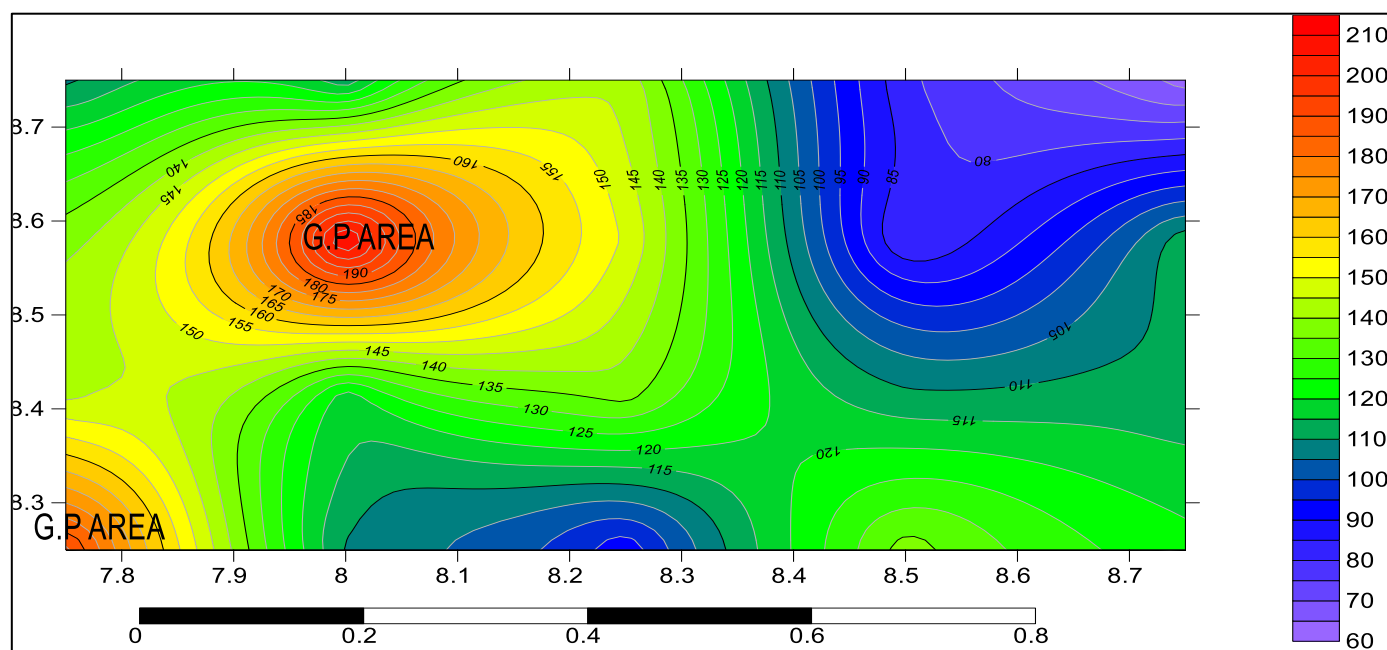


Fig 9: Geothermal Heat Production Distribution Map in the Research Area

The regions of Kuri, Nasarawa, and Indo have higher geothermal gradient values, whereas the regions of Achigogo, Alungane, Adogi, and Giringwe have lower values (Figure 9).

C. Radioelements Concentration and Ternary Map Concentration of Potassium (%)

The distribution of potassium (%) across the study area, as depicted in the plot, shows that the northeastern and northwestern regions are particularly rich in potassium. This aligns with the presence of porphyritic granites in the

geological map of the area. Additionally, the southwestern and southeastern edges also exhibit relatively high potassium concentrations.

The potassium distribution is depicted in Figure 10's contour map, where levels range from 0.9% to 4.2%. Amphibolite, banded gneiss, undifferentiated schist, granite gneiss, pegmatite/quartz veins, meta-volcanic rocks with pegmatite complexes, and porphyritic granite formations are among the geological groups to which these values match. The research area's potassium concentration ranges from a

low of -0.1% to a maximum of 4.20%, with an average of 0.48%.

Because of the area's varied lithological units and changes, the map shows different potassium concentrations. Potash feldspars, which are plentiful in felsic igneous rocks like granite but sparse in mafic rocks like basalts and andesites, are the main source of potassium radiation (Gunn et al., 1997b). Elevated potassium levels can also result from changes in rocks (Wilford et al., 1997). The radiometric image (Figure 10) makes potassium anomalies easily discernible. Low potassium values are represented by blue, very high potassium concentrations by pink, moderately high to high potassium values by red, and moderately low potassium levels by shades of orange to yellow.

The southern portion of the research area (designated as VL), which corresponds to the sandstone and shale sections

on the geological map (Figure 2), has low potassium contents. Water bodies concealing the potassium radiation from the underlying rocks is probably the cause of this low concentration, which lowers the signal's strength. The interference from the water body reduces the potassium signal because radiometric surveys presume that the top 30 cm of soil absorbs the majority of the radiated radioactive elements from the rocks or lithology below.

The northeastern, northwest, and southwestern regions of the region—designated as VH in Figure 10—have high potassium contents. The basement rocks, which contain granite gneiss, likewise match these regions. The basement rock regions depicted on the geological map (Figure 2) correspond to the elevated potassium levels in the northern portion of the research area. According to Osae *et al.* (2006), this indicates that the basement in this location has a high potassium concentration.

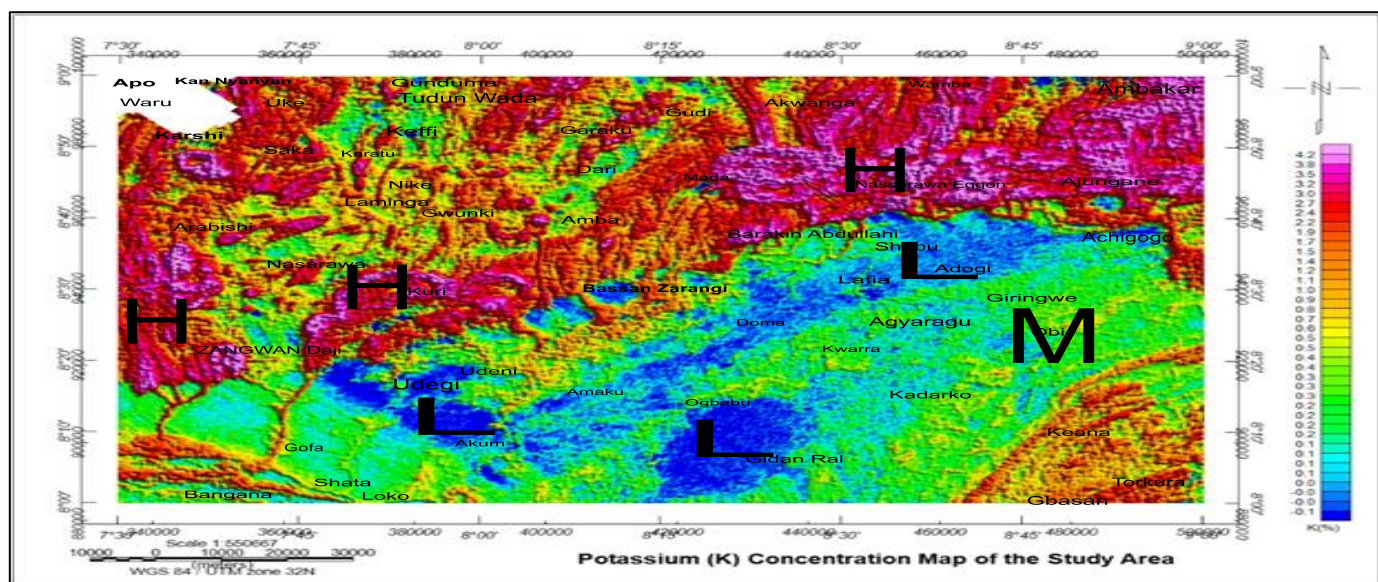


Fig 10: K (%) Conc. of the Area

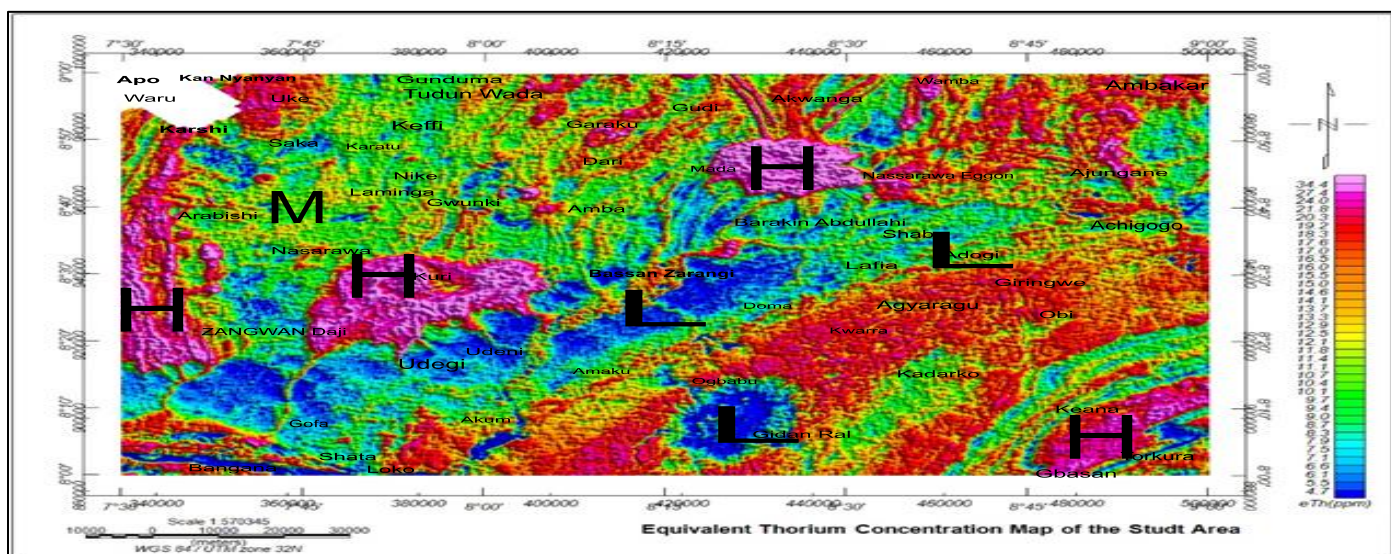


Fig 11: eTh Conc. of the Area

The southeast (SE) and southwest (SW) regions of the research area, which correspond to the Nkporo Formation and Eze-Aku Group, have comparatively low potassium (K) concentrations. The Residual Magnetic Intensity map (Figure 3b) clearly shows the sedimentary sandstone units, which are in line with this. The findings of Osae *et al.* (2006), who observed that sandstone and shale generally have low potassium contents, are corroborated by the low potassium levels in the sandstone. However, there is a small, almost linear area with elevated potassium values within the sandstone zone (Figure 10), which may be a structural characteristic. Elevated areas in the Digital Elevation Map (DEM) (Figure 2) also correspond with this greater potassium concentration, even though the lithological contacts are not distinctly visible in the potassium distribution map.

D. Thorium (Th) Concentration

Three distinct thorium concentration zones are depicted on the thorium concentration map (Figure 11): high concentrations are shown in pink, moderate concentrations are shown in green, and low concentrations are shown in blue. The DEM (Figure 2) indicates that the weathered sediments in the region are thought to have originated from sandstone in the higher elevation areas (Jones, 1990), and the high thorium concentrations (marked with a "P" in Figure 11) correspond

to the shale regions. The middle and southwestern portions of the region have a low thorium content (shown by a white polygon), which corresponds with the line separating the two main types of rocks: sedimentary rocks and basement rocks. The reason for this low concentration can be that the underlying lithology is shielded from the thorium radiation by a lake or other body of water. However, a higher clay content and the clay particles in these aged soils' ability to adsorb thorium are suggested by the strong thorium emissions (red color) in weathered sedimentary rocks from the elevated areas (Figure 2) (Blay, 2003).

E. Uranium Concentration

The uranium map (Figure 12) successfully highlights the Volta Lake area (indicated by a black polygon) and key geological structures like BSH and B. The uranium map exhibits the same circular pattern that is seen in the thorium and potassium maps, indicating high uranium concentrations (pattern "B"). This characteristic is consistent with the area's basaltic rocks as reported by Jones (1990). Furthermore, the middle portion of the region (shown by a white hexagon) exhibits a significant uranium concentration, which corresponds with the shale. Therefore, as seen by the white polygon in Figure 12, the shale zones are represented by relatively high uranium contents.

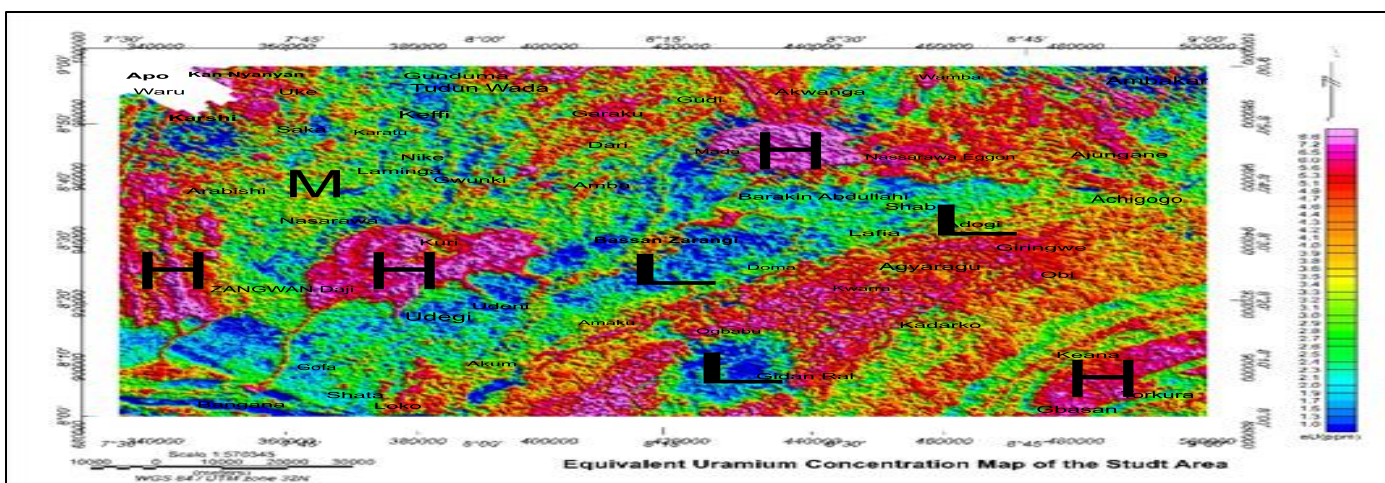


Fig 12: eU Concentration of the Area

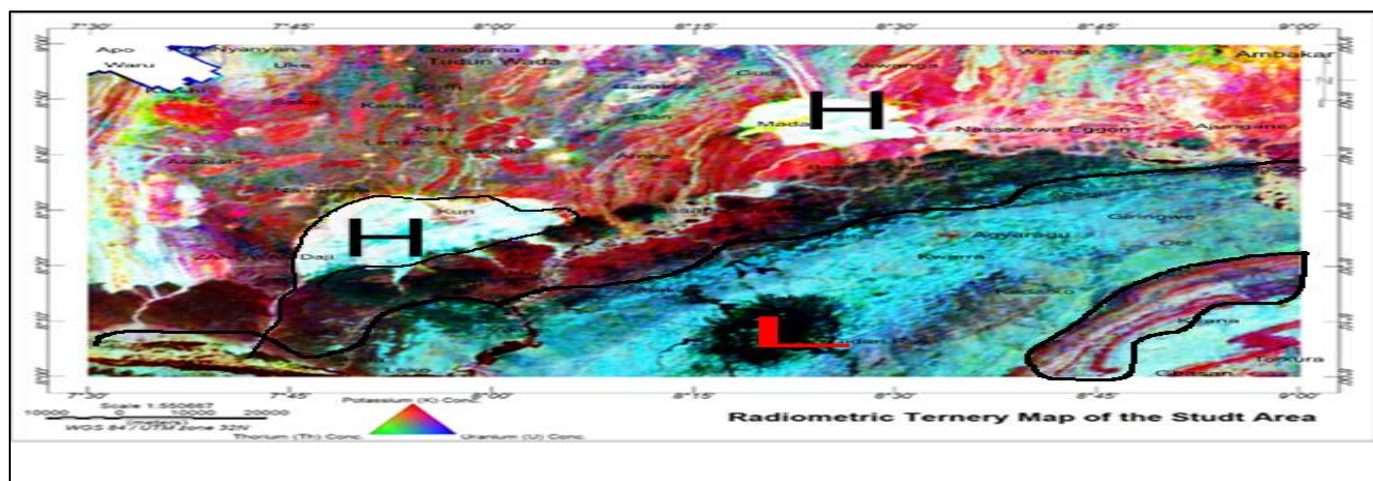


Fig 13: Ternary Map of the Area

The borders between the majorities of the lithological units in the region are not clearly depicted as opposed to the potassium (K) and thorium (Th) maps, on the uranium (U) map. For example, unlike the thorium (Figure 11) and potassium (Figure 10) maps, the uranium map lacks the clear demarcation between the sandstone and shale layers. The short wavelength aberrations observed in the uranium image (Figure 12) are caused by variations in air radon concentrations during the survey. These variations result in noticeable streaking in the uranium map even after the data has been processed, which is a common issue in uranium imaging (Minty, 1997).

F. Ternary Map of the Study Area

On the ternary map that shows the radiometric data, the combined intensities of uranium (U), thorium (Th), and potassium (K) concentrations are displayed as red, green, and blue, respectively. The K, Th, and U concentrations are represented by a number of color combinations on the ternary map (Figure 13). Generally speaking, this map's radiometric reactions correspond to the local surface geological features (Figure 2). Magenta indicates areas with high potassium and low amounts of uranium and thorium, whereas black indicates areas with low concentrations of U, Th, and K. Yellow locations show high uranium and thorium concentrations but low uranium, while green areas show low potassium but high uranium and thorium concentrations. Blue

regions are defined by low potassium and high uranium and thorium.

The Volta Lake, shown in black in Figure 13 on the ternary map, is clearly a location with low quantities of all three radiogenic elements. It is also possible to see where the sandstone and shale units meet. Black polygons indicate areas with high amounts of K, Th, and U; these areas correspond to shale and weathered sediment zones, as reported by Osae *et al.* (2006) and Jones (1990). Shale emits more gamma radiation than other sedimentary rocks in the region, according to these authors. The sandstone areas are in line with the magenta color, which indicates high potassium with low uranium and thorium. Interestingly, these places also occur in the study region's high elevation zones.

G. Analysis of Radioactive Heat Production: A Qualitative and Quantitative Approach

To determine the radiogenic heat production, a profile was created across the K, Th, and U radioelement maps. For this reason, the rock units were identified and assigned together with their average densities. Based on the concentrations of uranium, thorium, and potassium in each rock unit, these densities were then utilized to calculate the radioactive heat generation, as shown in equation (7). Table 2 provides a summary of the findings.

Table 2: Summary of Radiogenic Production Obtained from Sixteen Profiles Across the Study Area

S/N	Sections	Longitudes (°C)	Latitude (°C)	C_K (%)	C_{Th} (ppm)	C_U (ppm)	RHP ($\mu W/m^3$)
1	A	7.6	8.5	1.6	13.5	3.7	2.0345
2	B	7.7	8.5	1.0	10.9	3.0	1.6185
3	C	7.7	8.5	1.1	9.9	2.7	1.4817
4	D	7.8	8.5	0.9	12.9	3.3	1.8244
5	E	8.0	8.5	0.8	13.2	3.5	1.8872
6	F	8.1	8.5	0.7	11.7	3.4	1.7484
7	G	8.3	8.5	0.7	10.1	2.9	1.5093
8	H	8.5	8.5	1.2	15.5	4.4	2.3151
9	I	8.6	8.5	1.3	14.4	4.0	2.1456
10	J	8.7	8.5	0.9	15.1	4.2	2.2078
11	K	8.9	8.5	1.5	14.8	4.1	2.2178
12	L	8.2	8.5	1.5	11.0	2.5	1.5439
13	M	8.3	8.5	0.9	13.4	3.7	1.9618
14	N	8.2	8.9	1.9	13.6	3.8	2.0953
15	O	8.3	8.2	0.2	10.8	3.1	1.5621
16	P	8.3	8.6	0.8	12.0	3.2	1.7271
Minimum			0.2	9.9	2.5	1.48	
Maximum			1.9	15.5	4.4	2.32	
Average			1.06	12.68	3.47	1.87	

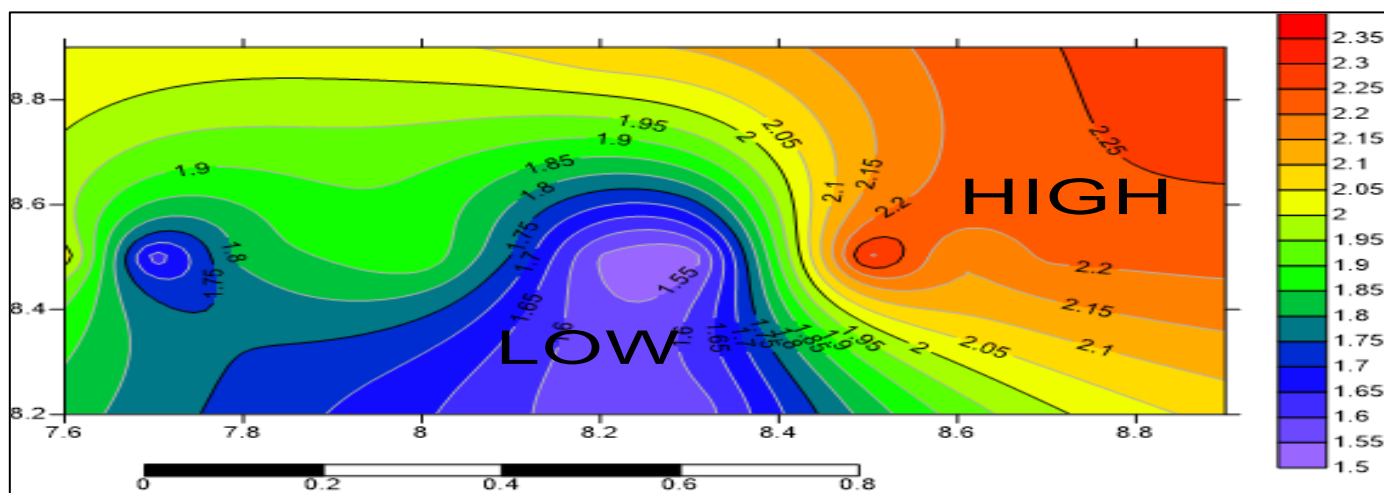


Fig 14: Radiogenic Heat Production Map Distribution of the Study Area

The rock units listed below were found in the study area: Alluvium, Sandstones, Shale and Sandy layers of the Lafia Wukari Formation, Quartzite, Porphyroblastic Schists (including Phyllites), Granite Gneiss, Porphyritic Granite, Unidentified Granite Migmatite, Shale Limestone of the Awgu Formation, Shale Mudstone of the Nkporo Formation, and The Eze-Aku Group includes sandstone, siltstone, and black shale. Additionally, Basalt, Trachyte, and Rhyolite were designated as Basic and Intermediate Intrusions based on their concentrations of potassium (K), thorium (Th), and uranium (U) and included in the computation of radiogenic heat generation. Table 2 provides a summary of each rock unit's radiogenic heat analysis results, while Figure 14 shows the radiogenic heat production map. The research area's northeastern (NE) and southeast (SE) sectors, especially the Lafia-Doma areas, showed high heat concentrations.

According to this study, radiogenic heat generation generally varies greatly based on the type of rock. The high link between the geology map (Figure 2) and the radiogenic heat production map (Figure 14) can be explained by this variability. Some statistical parallels can be seen in the average radiogenic heat production values for specific formations, including the Awgu Formation, Lafia Wukari, Eze Aku Shale Group, and Nkporo Shale. But even among rocks of the same type in different places, the study also discovered differences in radiogenic heat values. Due to variations in the geochemical behavior of uranium (U), thorium (Th), and potassium (K) throughout the metamorphic process, which affects the distribution of naturally occurring radio-elements, this irregularity can be explained (Salem et al., 2005). High uranium content correlates with high radiogenic heat output, suggesting that the abundance of uranium is primarily responsible for the high heat values in these areas. The range of radiogenic heat values in the research area is 1.48 to $2.32 \mu\text{Wm}^{-3}$, which is near the benchmark of $4 \mu\text{Wm}^{-3}$ for high generation of radiogenic heat (Alistair et al., 2014). Because of their higher levels of radiogenic heat production, the northeastern and southeast regions of the study area are regarded as hotspots, with radiogenic heat values that are closer to this benchmark.

V. CONCLUSION

Geothermal analysis confirmed the presence of significant geothermal sources, as evident on the geothermal heat flow distribution maps. Promising regions for geothermal heat sources are located around Lafia, Doma, and Awe, characterized by low Curie point depths, as indicated in the geothermal heat flow map and the Curie point depth map. These regions also fit the research area's geological characteristics.

Further work is recommended, including geochemical analysis and temperature variation studies, where rock samples can be collected and analyzed in the laboratory for more detailed investigation.

REFERENCES

- [1]. Bhattacharyya, B.K., & Leu, L.K. (1975). Analysis of Magnetic Anomaly Over Yellowstone National Park: Mapping of Curie point isothermal surface for Geothermal Reconnaissance. *Journal of Geophysical Research*. vol. 8, pp. 4461-4465.
- [2]. Blakely, R.J. (1995). *Potential Theory in Gravity and Magnetic Applications*. Cambridge University, Cambridge.
<http://dx.doi.org/10.1017/CBO9780511549816>.
- [3]. Jaques, A.L., Wellman, P., Whitaker, A., & Wyborn, D. 1997. High resolution geophysics in modern geological mapping. *AGSO Journal of Australian Geology and Geophysics*. Vol.17, pp.159-174.
- [4]. Jessop, A.M. (1990). *Thermal geophysics*, Elsevier, Amsterdam.
- [5]. Mero, J.L. (1960). Uses of the gamma-ray spectrometer in mineral exploration. *Geophysics*, 25:1054-1076.
- [6]. Myers, K.J., & Bristow, C.S. (1989). Detailed sedimentology and Gamma-ray log characteristics of a Namurian Deltaic succession II: Gamma-ray logging. *Geology Society London Special Publication*. 136:1-7.

- [7]. Nwankwo, L.I., Olasehinde, P.I., & Akoshie, C.O., (2011). Heat flow anomalies from the spectral analysis of airborne magnetic data of Nupe Basin, Nigeria. *Asian Journal of earth science*. vol. 1, no. 1, pp. 1-6.
- [8]. Okubo, Y., Tsu, H. & Ogawa, K. (1985). Estimation of Curie point temperature and geothermal structure of island arcs of Japan. *Elsevier Science Publishers, Tectonophysics*, 159. 279-290.
- [9]. Onwuemesi, A.G. (1997). One-Dimensional Spectral Analysis of Aeromagnetic Anomalies and Curie Depth Isotherm in the Anambra Basin of Nigeria. *J. Geodynamics*. 23(2), 95-107.
- [10]. Rybach, L. (1996). Radioactive Heat Production in Rocks and its Relation to other Petrophysical parameters. *Pure and Appl Geophysics* 114: 309-318.
- [11]. Rybach, L., & Schwarz, G.F. (1995). Ground Gamma Radiation Maps: Processing of airborne, laboratory, and *in situ* spectrometry data. *First Break* 13: 97-104.
- [12]. Salem, A., Abouelhoda, E., Alaa, A., Atef, I., & Sachio, E. (2005). Mapping radioactive heat production from airborne spectral gamma-ray data of Gebel Duwi Area, Egypt. *Proceedings World Geothermal Congress, Antalya, Turkey*, 24-29.
- [13]. Sanderson, D., East, B., & Scott, E. (1989). Aerial radiometric survey of parts of North Wales in July 1989; Scottish Universities Research and Reactor Centre: Glasgow, UK.
- [14]. Shi, Z., & Butt, G. (2004). New Enhancement Filters for Geological Mapping. *ASEG Extended Abstracts*, 2004:1, Pp. 1-4, DOI: 10.1071/ASEG2004ab129.
- [15]. Spector, A. & Grant, F. S. (1970). Statistical Models for Interpreting Aeromagnetic Data. *Geophysics*, Vol. 35, pp. 293–302.
- [16]. Tanaka, A., & Ishikawa, Y. (2005). Crustal thermal regime inferred from magnetic anomaly data and its relationship to seismogenic layer thickness: The Japanese islands case study. *Phys. Earth Planet. Inter.* 152:257-266.
- [17]. Tanaka, A., Okubo, Y., & Matsubayashi, O. (1999). Curie point depth base on spectrum analysis of the magnetic anomaly data in East and Southeast Asia. *Tectonophysics*, 306:461-470.
- [18]. Telford, W., Gelbert, I., & Sheritt, R. (1990). *Applied Geophysics* (Second ed.) London: Cambridge University Press.
- [19]. Thompson, P.H., Judge, A.S., Charbonneau, B.W., Carson, J.M., & Thomas, M.D. (1996). Thermal regimes and diamond stability in the Archean Slave Province, Northwestern Canadian Shield, District of Mackenzie, Northwest Territories; in *Current Research*, 96-1E, Geological Survey of Canada, pp. 135-146.
- [20]. Charbonneau, B.W., Holman, P.B., & Hetu, R.J. 1997. Airborne gamma spectrometer magnetic-VLF survey of northeastern Alberta. In *Exploring for minerals in Alberta*. Geological Survey of Canada Geoscience contributions, edited by MacQueen, Canada-Alberta agreement on mineral development. *Geological Survey of Canada Bulletin*. Vol. 500, pp. 107-132.
- [21]. Darnley, A.G. (1990). International geochemical mapping: a new global project. *Journal of Geochemical Exploration*. 39(1):1-13. DOI:10.1016/0375-6742(90)90066-J.
- [22]. Energy Commission of Nigeria (2012). *Energy Commission of Nigeria: Renewable Energy Master Plan*, Abuja, Nigeria.
- [23]. Udensi, E.E., & Osazuwa, I.B. (2004). Spectral determination of depths to magnetic rocks under the Nupe Basin, Nigeria. *Nigerian Association of Petroleum Explorationists (NAPE) Bull.* 17:22-27.
- [24]. Ravat, D., Pignatelli, A., Nicolosi, I., & Chiappini, M. (2007). A study of spectral methods of estimating the depth to the bottom of magnetic sources from near-surface magnetic anomaly data. *Geophysical Journal International*. Vol. 169, (2007). pp. 421– 434.
- [25]. Reiter, M.A., & Jessop, A.M. (1985). Estimates of terrestrial heat flow in offshore Eastern Canada. *Can J Earth Sci* 22: 1503-1517.
- [26]. Fernández, M., Marzan, I., Correia, A., & Ramalho, E. (1998). Heat flow, heat production and lithosphere thermal regime in the Iberian Peninsula, *Tectonophysics* 291, 29-53.
- [27]. Gunn, P., Maidment, D., & Milligan, P. (1997a). Interpreting Aeromagnetic Data in areas of limited outcrop. *AGSO Journal of Australian Geology & Geophysics*. 17(2), 175–185.
- [28]. Graham, D.F., (1993). Airborne radiometric data a tool for reconnaissance geological mapping using a GIS Thematic Conference. In: *Proceedings, 9th, Geologic Remote Sensing*, vol. 1, Pasadena, CA, February 8–11, 1993, pp. 43–54.
- [29]. Davies, S., & McLean, D. (1996). Spectral gamma-ray and palynological characterization of Kinderscoutian marine bands in the Namurian of the Pennine Basin. *Proc. Yorks. Geol. Polytech. Soc.* 51:103-114.
- [30]. Richardson, K.A., Killeen, P.G. (1980). Regional Radioactive heat production mapping by airborne gamma-ray spectrometry; in *Current Research, Part B*, Geological Survey of Canada, Paper 80-1B, pp. 227-23.